



**HAL**  
open science

## 3D interaction diagrams for symmetrically reinforced concrete square sections with various reinforcement ratios

Androniki-Anna Doulgeroglou, Panagiotis Kotronis, Giulio Sciarra, Catherine Bouillon

### ► To cite this version:

Androniki-Anna Doulgeroglou, Panagiotis Kotronis, Giulio Sciarra, Catherine Bouillon. 3D interaction diagrams for symmetrically reinforced concrete square sections with various reinforcement ratios. *Engineering Structures*, 2022, 262, pp.114272. 10.1016/j.engstruct.2022.114272 . hal-03666644

**HAL Id: hal-03666644**

**<https://hal.science/hal-03666644>**

Submitted on 6 May 2023

**HAL** is a multi-disciplinary open access archive for the deposit and dissemination of scientific research documents, whether they are published or not. The documents may come from teaching and research institutions in France or abroad, or from public or private research centers.

L'archive ouverte pluridisciplinaire **HAL**, est destinée au dépôt et à la diffusion de documents scientifiques de niveau recherche, publiés ou non, émanant des établissements d'enseignement et de recherche français ou étrangers, des laboratoires publics ou privés.



Distributed under a Creative Commons Attribution - NonCommercial 4.0 International License

# 3D interaction diagrams for symmetrically reinforced concrete square sections with various reinforcement ratios

Androniki-Anna Doulgeroglou<sup>a,b,\*</sup>, Panagiotis Kotronis<sup>a</sup>, Giulio Sciarra<sup>a</sup>,  
Catherine Bouillon<sup>b</sup>

<sup>a</sup>*Nantes Université, Ecole Centrale Nantes, CNRS  
Institut de Recherche en Génie Civil et Mécanique (GeM),  
UMR 6183, F-44000 Nantes, France.*

<sup>b</sup>*Groupe Essor,  
2 rue Pierre Gilles de Gennes 64140 Lons, France.*

---

## Abstract

3D interaction diagrams for symmetrically Reinforced Concrete (RC) square sections with various reinforcement ratios are constructed using 3D non-linear finite element simulations. The interaction diagrams are expressed in terms of generalized forces (axial force, bending moment and shear force) and allow to identify two characteristic states: the first characteristic state corresponds to the elastic limit of the reinforcement bars (while concrete exhibits a non-linear behavior) and the second characteristic state to the peak values of the generalized forces generalized displacements curves. Firstly, 3D non-linear finite element simulations of RC cantilever - type columns are presented and validated with experimental results.

---

\*Corresponding author.

*Email address:* Androniki-Anna.Doulgeroglou@ec-nantes.fr (Androniki-Anna Doulgeroglou)

Numerical interaction envelopes are then derived and analytical convex expressions are provided. Finally, a comparison with existing interaction diagrams from the literature is proposed.

*Keywords:* interaction diagrams; reinforced concrete.

---

## **1. Introduction**

Interaction diagrams are functions that define the acceptable combinations of generalized forces' components (e.g. moment, shear force and axial force) of a structural member. Of particular interest in Reinforced Concrete (RC) design they are often constructed using limit analysis. To characterize the combination of axial force and bending moment limit states, in the Eurocode [1] a suitable set of admissible loadings, is identified for a given RC structure and a convex hull of them is constructed adopting the so-called lower bound approach. More specifically, steel is described by an elastic perfectly plastic constitutive law, symmetric in traction and compression, while concrete has zero tension resistance and follows a parabolic curve in compression. A rectangular distribution of the normal stress is assumed, multiplied by a correction factor. Eurocode [1] provides also interaction diagrams for biaxial bending and axial loading and for shear force and torsion but not for axial force, shear force and bending moment.

In the framework of limit analysis the upper bound approach is also frequently used which provides an upper bound of a combination of the limit loadings, see e.g. [2]. The definition of limit loading in this case is based on a global energetic criterion which compares the power dissipated along a plastic process to the power

of external forces. It is typically used introducing kinematically admissible velocity fields exhibiting a jump through the body which is therefore separated into two blocks having a relative motion one with respect to the other. If a kinematic admissible mechanism can be found for which the work of the external loads exceeds the internal work, then the structure collapses and the load computed on the basis of the assumed mechanism is greater than or equal to the true failure load. The limit load is determined by searching for the least upper bound for loads inducing collapse. In literature, this method is used to study failure of beams and plates. Koechlin [3] introduced a global failure criterion for RC beams considering coupled loading of axial force and bending moment. This criterion was extended to plates by accounting for combination of membrane forces and bending moments. In a subsequent work, Koechlin [4] derived a failure criterion for beams submitted to a combination of axial force, shear force and bending moment.

It is possible to construct interaction diagrams by numerical methods or combining analytical and numerical methods. Elachachi [5] used a multi-fiber beam finite element model to reproduce the bending moment - axial force interaction diagram for a reinforced concrete structure (for zero shear force) and constructed the moment - shear force diagram for zero axial force.

Vecchio and Collins [6] combined analytical and numerical approaches. The analytical framework is based on the Modified Compression Field Theory (MCFT), formulated for in-plane stress conditions [7] that relates average stress to average strains in a cracked RC element, satisfying compatibility and equilibrium requirements. The authors present interaction diagrams for shear force and bending mo-

ment for different axial loads and interaction diagrams for shear force and axial force.

Rahal [8] proposed a simplification of the MCFT assuming a parabolic stress-strain relationship for concrete in compression and provided a graphical method to compute the ultimate shear strength of members. In a subsequent work [9], the author extended the method to beams under combined shear, bending and axial load.

Nguyen [10] constructed interaction diagrams for the following loading combinations: bending moment and torsion, bending moment and shear force, coupled shear force - bending moment - torsion. The author developed a 3D multi-fiber beam element that takes into account warping. The cross-section is divided into three zones (named 1D, 2D and 3D) according to the direction of transversal reinforcement and the stress state.

Carpinteri et al. [11] studied the influence of size scale effects on the moment - axial force interaction diagrams using a numerical step-by-step approach based on the integrated Cohesive/Overlapping Crack Model. Constitutive modeling of concrete is different in compression (Overlapping Crack Model with fictitious interpenetration) and tension (Cohesive Crack Model with fictitious crack). Stress-displacement relationships are adopted for the post-peak behavior to avoid scale dependency.

In the following, we present 3D interactions diagrams for symmetrically reinforced concrete square sections constructed using 3D non-linear finite element calculations without adopting any kinematic assumptions and that take into con-

sideration an accurate description of the constitutive modeling of the materials and stress redistributions . The contribution of this work relies on estimating the ultimate resistance of a RC section which is different than the Ultimate Limit State (ULS) found in the design codes. The interaction diagrams are expressed in terms of generalized forces (axial force, bending moment and shear force). Another advantage of the numerical simulations is that access is provided to any intermediate state of the response during loading and thus they allow to identify two characteristic states: the first characteristic state corresponds to the elastic limit of the reinforcement bars (while concrete exhibits a non-linear behavior) and the second characteristic state to the peak values of the generalized forces generalized displacements curves. The purpose of the identification of these characteristic states is to use them in a future work for the development of a macro-element for reinforced concrete beam and columns, in the light of what has been already done for example for shallow foundations ([12], [13], [14]) and piles ([15], [16], [17]).

The article is structured as follows: section 2 presents the adopted 3D constitutive models for concrete and steel; in section 3 the 3D finite element model is validated with reference to the experimental results of a RC cantilever - type column submitted to complex loading [18]. After establishing the criteria for the two characteristic states, numerical interaction envelopes for a specific RC section are derived in section 4 and this procedure is repeated for the construction of numerical interaction envelopes for symmetrically reinforced concrete square sections with different reinforcement ratios in section 5. Analytical convex expressions of these surfaces are finally introduced in section 6 and a comparison

with interaction diagrams from the Eurocode [1] is proposed in section 6.6.

## 2. Constitutive models

### 2.1 Concrete

Concrete behavior is described by the 3D constitutive model developed by Faria et al. [19]. The model follows the damage mechanics framework and is coupled with plasticity to consider inelastic permanent strains in compression. The 3D (effective) stress tensor is defined by:

$$\bar{\sigma}(\varepsilon, \varepsilon^p) = D_0 : (\varepsilon - \varepsilon^p) \quad (1)$$

where  $D_0$  is the fourth-order isotropic linear elastic constitutive matrix,  $\varepsilon$  is the strain tensor and  $\varepsilon^p$  is the plastic strain tensor. Stress contributions due to tension or compression are expressed by splitting the effective stress tensor into tensile  $\bar{\sigma}^+$  and compressive  $\bar{\sigma}^-$  components:

$$\bar{\sigma}^+ = \sum_i \langle \bar{\sigma}_i \rangle p_i \otimes p_i \quad (2)$$

$$\bar{\sigma}^- = \bar{\sigma} - \bar{\sigma}^+ \quad (3)$$

where  $\bar{\sigma}_i$  is the  $i_{th}$  principal stress,  $p_i$  is the unit vector corresponding to the  $i_{th}$  principal direction,  $\langle \cdot \rangle$  are the Macaulay brackets and indices (+) and (-) correspond to positive and negative entities.

Even though it does not account for permanent strains during tension, the

model is able to reproduce the differences in the behavior in tension and compression using two scalar damage variables which are assumed to correspond to independent processes. Two damage criteria are considered:

$$\bar{\tau}^+ = \sqrt{\bar{\sigma}^+ : D_0^{-1} : \bar{\sigma}^+} \quad (4)$$

$$\bar{\tau}^- = \sqrt{\frac{\sqrt{3}}{3}KI_1 + \sqrt{2J_2}} \quad (5)$$

where  $\bar{\tau}^+$  and  $\bar{\tau}^-$  are the tensile and compressive equivalent stress respectively,  $I_1$  and  $J_2$  are the first invariant of the compressive stress tensor and the second invariant of the deviatoric compressive stress tensor respectively and  $K$  is a material parameter conceived to fit the ratio of 2D and 1D compressive strengths  $\sigma_{c,2D}/\sigma_{c,1D}$  in experimentally observed values (1.16-1.2). The model accounts for the increase of concrete strength when biaxial or triaxial compressive loading conditions are considered.

The unilateral effect, also known as stiffness recovery, takes place as the load changes sign and results in tensile cracks' closure and gradual compressive stiffness recovery. This model takes into account the unilateral effect in a simplified way (no permanent strains during traction unloading and no progressive stiffness recovery).

The evolution laws for the damage variables in tension and in compression are given by:

$$d^+ = G^+(r^+) = 1 - \frac{r_0^+}{r^+} e^{A^+(1-r^+/r_0^+)} \quad (6)$$

$$d^- = G^-(r^-) = 1 - \frac{r_0^-}{r^-} (1 - A^-) - A^- e^{B^-(1-r^-/r_0^-)} \quad (7)$$

where  $r^+$  and  $r^-$  are the current damage thresholds,  $r_0^+$  and  $r_0^-$  are the elastic thresholds,  $A^+$  controls the softening response in tension and  $A^-$  and  $B^-$  define the non-linear part of the response in compression.

The plastic strain tensor rate in compression is given by:

$$\dot{\varepsilon}^P = \beta EH(d^-) \frac{\langle \bar{\sigma} : \dot{\varepsilon} \rangle}{\bar{\sigma} : \bar{\sigma}} D_0^{-1} : \bar{\sigma} \quad (8)$$

where  $\beta \geq 0$  is a material parameter which controls the rate intensity of plastic deformation and  $H$  is the Heaviside function. The consideration of plastic strains during compression and of the unilateral effect makes the constitutive law appropriate for cyclic loading.

Mesh objectivity (in tension but not in compression) is taken into account via an energy type approach [20] that requires that the tension softening branch (parameter  $A^+$ ) is calibrated according to the tensile fracture energy and a geometrical characteristic length:

$$A^+ = \left( \frac{G_f E}{l_{ch} (f_0^+)^2} - \frac{1}{2} \right)^{-1} \geq 0 \quad (9)$$

where  $G_f$  is the tensile fracture energy,  $E$  is the Young's modulus,  $f_0^+$  is the tensile elastic limit,  $l_{ch}$  is a geometrical characteristic length computed as  $\sqrt[3]{\Delta V}$  with  $\Delta V$  the finite element volume in 3D simulations. Although this approach is not able to regularize the results in the local level, results in terms of forces and displacements

are less sensitive to the finite element mesh discretization [21].

Fig. 1 depicts the constitutive model during a 1D tension-compression cyclic test, while Fig. 2 the comparison with the biaxial plane stress experiments of [22]. From the latter, it can be seen that the constitutive law reproduces satisfactorily the biaxial strength of concrete and this for all biaxial loading conditions.

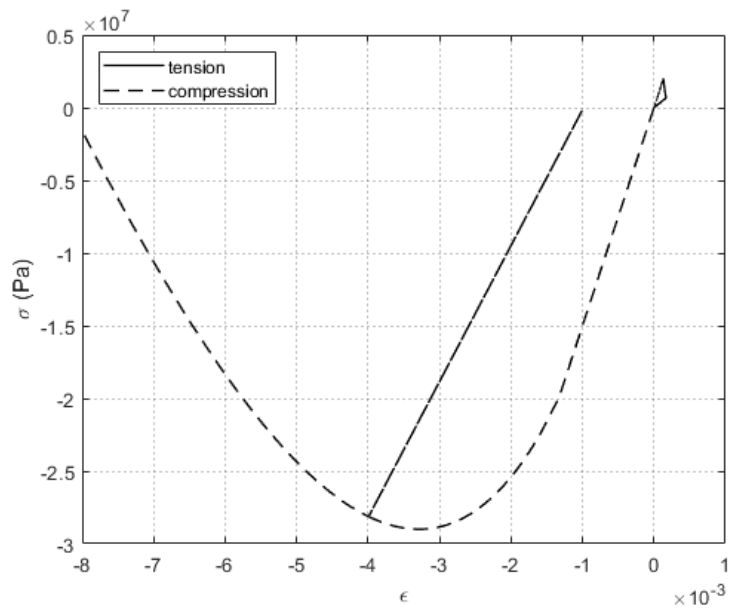


**Fig. 1.** Cyclic behavior during 1D cyclic test.

## 2.2 Steel

The classical 3D Von Mises elastoplastic law is considered for the reinforcement bars. A linear kinematic hardening is adopted to capture the Bauschinger effect observed during cyclic loading.

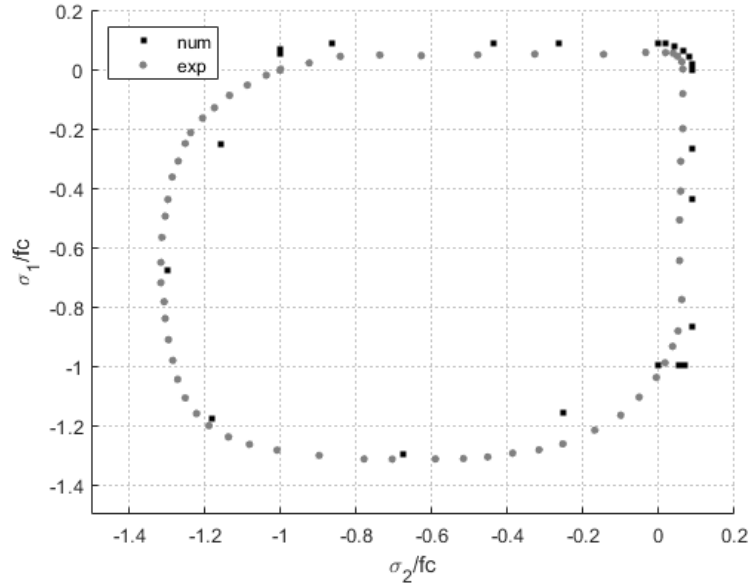


**Fig. 2.** Comparison of the numerical and experimental biaxial strength of concrete normalized by the uniaxial concrete compressive strength  $f_c$  [22].

### 3. Structural model validation: a reinforced concrete column under complex loading

In order to validate the 3D finite element model used in section 4 to construct the interaction diagrams, the reinforced concrete cantilever - type columns, studied experimentally by Bousias et al. [18] under various loading combinations, are simulated hereafter. During this campaign the researchers studied the behavior of twelve identical columns under cyclic uniaxial or biaxial flexure with constant or time varying axial load. The only test variable was the load path and the concrete compressive strength. The specimens were similar to those tested by Gutierrez et al. [23]. The geometry of the specimens is represented in Fig. 3.

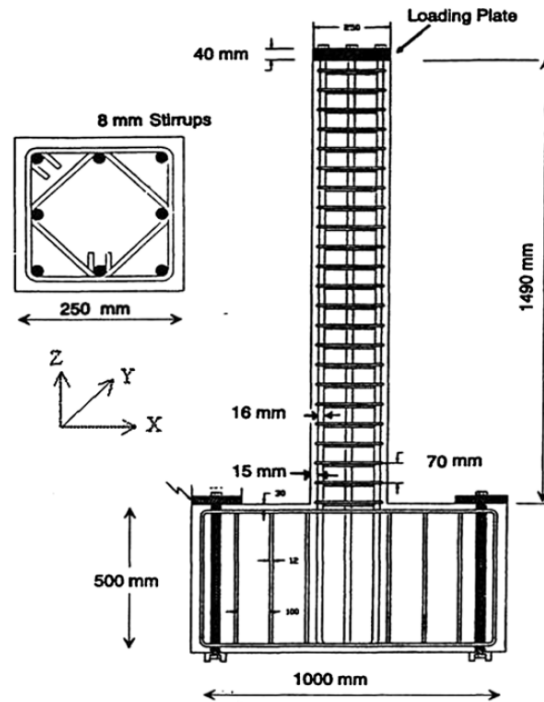


**Fig. 3.** RC columns: geometry, [23].

3D volumetric finite elements are used for the numerical simulations with the code Cast3M [24]. All the components of the reinforced concrete column are discretized; concrete, longitudinal reinforcing steel bars and stirrups. Perfect bonding is assumed between concrete and steel. The finite element mesh of each component is constructed independently. Displacement compatibility of the different components is ensured by forcing every point of the steel mesh to follow a linear combination of the nodal displacements of the concrete mesh. This approach results into an additional structural stiffness, which in our case is proved to be negligible (see Appendix A). A mesh of 10560 3D finite elements is adopted and this choice is explained in further details in Appendix B. The Newton-Raphson

Test Specimen	$f'_c$	$N/(A_c f'_c)$	Load Path
S6	25.7	0.10	
S8	25.4	0.11	Shrinking 

**Table 1.** RC columns: test specimens, compressive strength, applied axial load and transversal load (schematically).

algorithm is adopted at the global level for the resolution of the non-linear system of equations. The radial return algorithm and the backward-Euler scheme is used for the integration of the constitutive law.

During the experimental campaign, the columns were built in a heavily reinforced foundation base. The numerical model is considered therefore fixed at the bottom. The choice of 3D numerical models for concrete and steels allows considering complex indirect phenomena such as the confinement of concrete inside the stirrups, which leads to an increased concrete strength.

The S6 and S8 tests are simulated hereafter. Loading is applied on the top of the column in two steps; firstly, the axial compressive load is applied as a force of negative sign in the  $z$  direction and it is equally distributed to all the nodes of the section at the top. Secondly, the transversal load along  $x$ ,  $y$  is applied as a displacement homogeneous for all the nodes of the section at the top. The loading program of S6 and S8 is presented in Table 1.

The parameters for the concrete constitutive law are listed in Table 2 and Table 3 and for steel in Table 4. Calibration of the non-linear concrete response

in compression is achieved by selecting two points of the curve representing the uniaxial response in compression; point 1 ( $\epsilon_{c1}, \sigma_{c1}$ ) and point 2 ( $\epsilon_{c2}, \sigma_{c2}$ ). The selected points vary for every test simulated resulting to different resistances in compression according to the experimental values. The reference stress  $\sigma_{cp}$  and strain  $\epsilon_{cp}$  are used for the determination of the material parameter  $\beta$  as shown in Eq. 10 [25]:

$$\beta = \frac{(E\epsilon_{cp} - \sigma_{cp})f_{cu}}{(E\epsilon_{cp} - f_{c0})(\sigma_{cp} + f_{cu})} \quad (10)$$

As stated in section 2.1  $\beta$  is a material parameter which controls the rate intensity of plastic deformation. As the ratio  $\sigma_{cp}/\epsilon_{cp}$  increases,  $\beta$  decreases and the permanent plastic strains during unloading are less important. Conversely, as the ratio  $\sigma_{cp}/\epsilon_{cp}$  decreases,  $\beta$  increases and the permanent plastic strains during unloading are more significant. When  $\beta$  tends to zero the model turns to a purely damage model in compression and the coupling to plasticity vanishes.

Fig. 4 and Fig. 5 present the numerical simulation results of the S6 and S8 tests. After concrete cracking and during alternate loads, the global response is mainly controlled by the reinforcement steel bars. The parameters for the steel constitutive law have been taken as reported in the experimental campaign of Bousias et al.(1995). The obtained prediction accuracy can be certainly improved using a more advance 3D constitutive model instead of the classical 3D Von Mises constitutive model with linear kinematic hardening. The purpose of the work being however the numerical computation of 3D interaction diagrams up to failure

Parameter	Description	SI Unit	Value
$E_b$	Young Modulus	$GPa$	15
$\nu_b$	Poisson's ratio	-	0.2
$f_t$	Elastic stress limit in tension	$MPa$	2
$G_f$	Tensile fracture energy	$J/m^2$	100
$l_{car}$	Characteristic length	$m$	$\sqrt[3]{jaco}$
$f_{c0}$	Elastic stress limit in compression	$MPa$	-20
$rt_{45}$	Biaxial ratio $\sigma_{c,2D}/\sigma_{c,1D}$ in compression	-	1.18
$f_{cu}$	Ultimate stress limit in compression	$MPa$	-35
$\epsilon_{cu}$	Ultimate strain in compression	-	-0.0035
$\sigma_{cp}$	Reference stress in compression	$MPa$	-33
$\epsilon_{cp}$	Reference strain in compression	-	-0.0044
$\epsilon_{c1}$	Strain of point 1	-	-0.002
$\epsilon_{c2}$	Strain of point 2	-	-0.005

**Table 2.** RC columns: parameters for concrete (constant for all the tests).

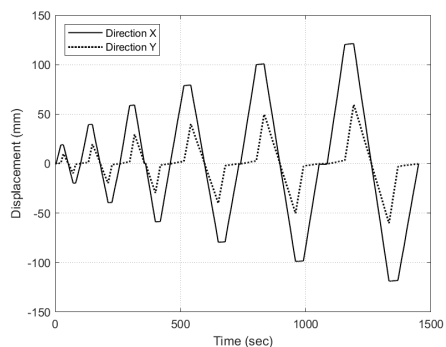
Parameter	$\sigma_{c1}$	$\sigma_{c2}$
Description	Stress of point 1	Stress of point 2
SI Unit	$MPa$	$MPa$
S6	-23.6	-22.6
S8	-23	-22

**Table 3.** RC columns: parameters for concrete (varying for each test).

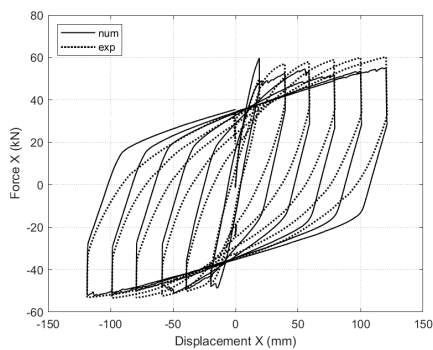
Parameter	Description	SI Unit	Value
$E_a$	Young Modulus	$GPa$	180
$\nu_a$	Poisson's ratio	-	0.3
$f_y$	Elastic stress limit	$MPa$	460
$H_a$	Kinematic hardening modulus	$GPa$	2.3

**Table 4.** RC columns: parameters for steel.

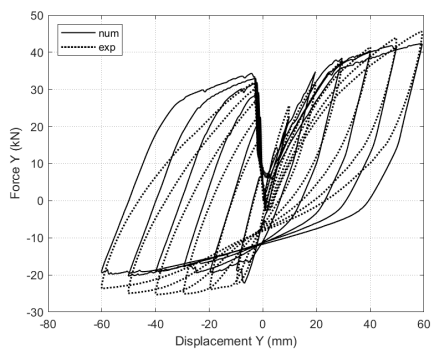
and not the cyclic behavior, the level of accuracy, as far as the peak of the response is concerned, is judged satisfactory; the 3D finite element model correctly reproduces the global behavior of the column in terms of forces - displacements and this for all the loading combinations and tests.



(a) Loading history

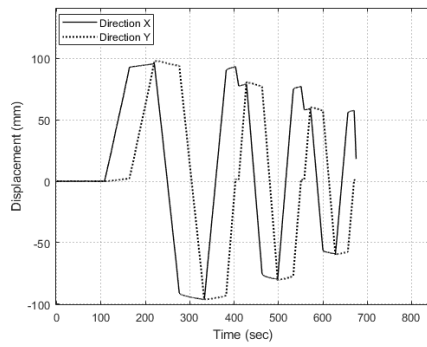


(b) Force - displacement, X direction

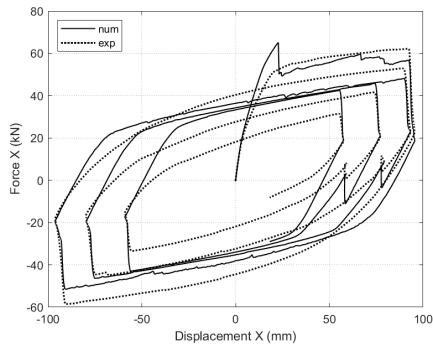


(c) Force - displacement, Y direction

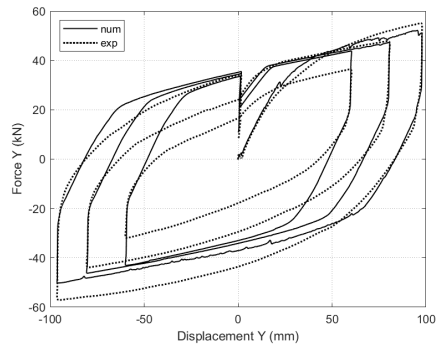
**Fig. 4.** Test S6: Numerical vs. experimental results.



(a) Loading history



(b) Force - displacement, X direction



(c) Force - displacement, Y direction

**Fig. 5.** Test S8: Numerical vs. experimental results.

#### **4. Interaction diagrams for a symmetrically RC square section**

For the construction of the interaction diagrams the validated numerical model of section 3 is adopted. The column is again considered fixed at the bottom and specific displacement loading combinations, described in section 4.2 are applied on its free top surface. Interaction diagrams are presented for different characteristic states, detailed hereafter.

##### *4.1 Characteristic states*

The interaction diagrams presented in this article are defined for the following two characteristic states:

- 1<sup>st</sup> characteristic state: corresponds to the elastic domain of the reinforcement steel bars (identical in tension and compression) fixed to  $460\text{MPa}$ .
- 2<sup>nd</sup> characteristic state (termed hereafter ‘failure’): corresponds to the peak values of the generalized forces-generalized displacement curves. More specifically, for the combined flexion to tension area, the failure criterion, is given in terms of maximum longitudinal steel strain equal to 7.5%, see also [1]. For the combined flexion to compression region, failure is reached at the maximum axial force (absolute value). This choice is made because the imposition of a criterion in terms of concrete maximum compression stress leads to very conservative estimations, as the maximum axial force is reached after several material points have attained their ultimate resistance.

The driving idea behind the choice of those two characteristic states is that steel controls the behavior of the reinforced concrete composite section when tension is predominant, while in compression, concrete crushing is considered to limit the buckling risk.

#### 4.2 Loading program

The displacement controlled loading program follows the swipe and radial tests commonly used in geotechnical engineering, see for example [26], [27]. The following loading conditions are applied:

- 1D loading: pure tension and pure compression in order to obtain the uniaxial section resistance (Fig. 6).

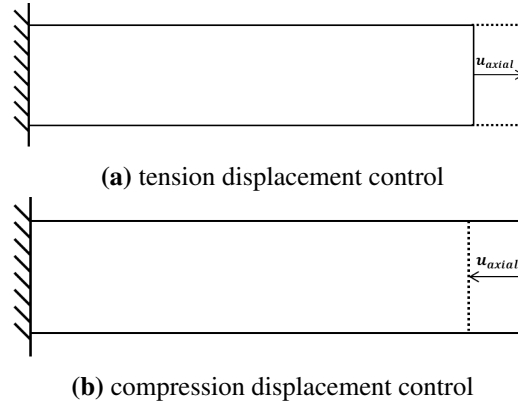


**Fig. 6.** Uniaxial loading.

- 2D loading: combined flexion with axial loading. The procedure is repeated in two ways; for the 2D swipe tests, an axial load is first applied followed by a flexure load (Fig. 7). The same procedure is repeated for different

levels of axial loading. The axial load is applied similarly to the case of 1D loading, while the flexural load is applied as a linear distribution of axial displacements, see Fig. 7.

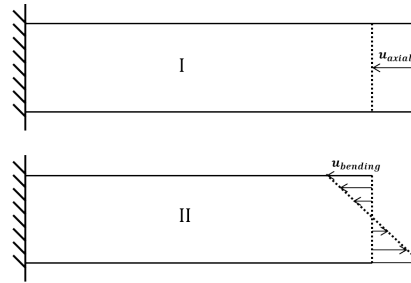


**Fig. 7.** 2D swipe test: I: axial loading, II: radial bending loading.

For the radial displacement controlled tests, the axial and flexural loads are applied simultaneously (Fig. 8) by keeping their ratio constant. The procedure is repeated for different ratios. The moment - axial force interaction diagram is obtained by both procedures and the results are compared to verify the influence of the loading path, which is found negligible.

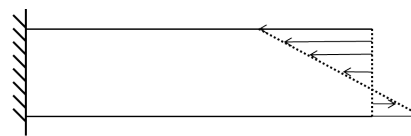


**Fig. 8.** 2D radial test: coupled bending - axial loading.

- 3D loading: for different levels of axial loading, flexural and transversal loads (controlled in displacements) are simultaneously applied in a radial way (constant ratio), as presented in Fig. 9. Thus, the complete moment – axial force – shear force diagram is obtained. Additional radial tests (all

loads are applied simultaneously) are also performed to verify the influence of the loading path. It is again found that the interaction diagrams are not significantly affected by the loading path.

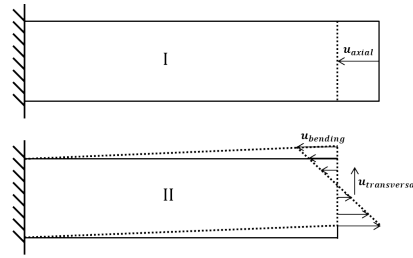
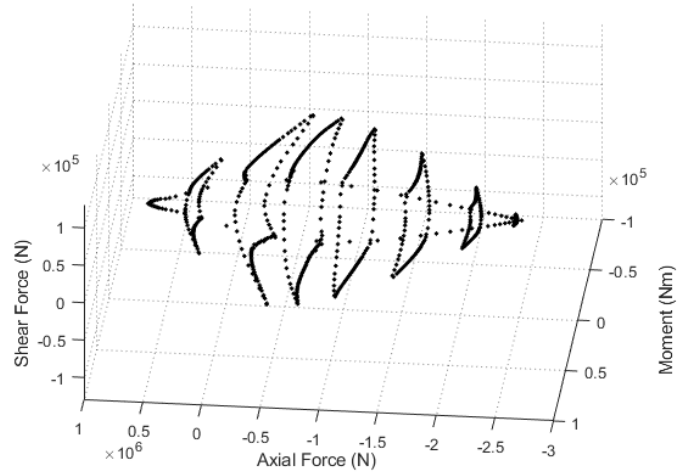


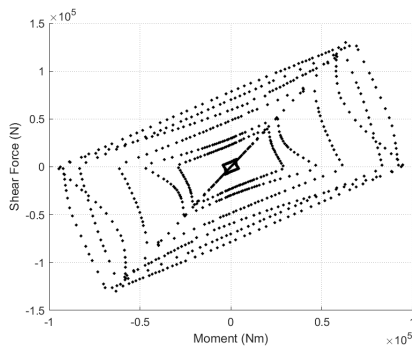
**Fig. 9.** 3D loading: I: axial loading, II: radial bending and shear loading by keeping constant the ratio  $\frac{u_{bending}}{u_{transversal}}$

### 4.3 Results

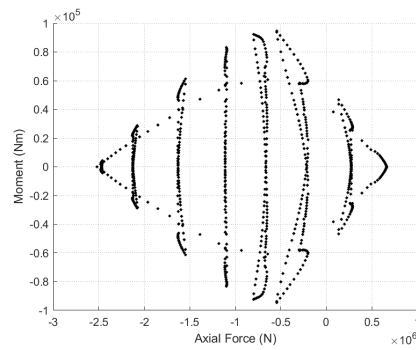
The data obtained by numerical simulations correspond to the points of the elastic domain of the reinforcing steel (Fig. 10) and to the discrete failure points (Fig. 11) respectively. By the application of uniaxial, 2D and 3D loading conditions the moment - axial force - shear force interaction diagrams are produced and correspond to the inner section of the column, at  $0.3m$  from the fixed edge. This section is found to be the most charged, is sufficiently far from the fixed edge (its distance from the fixed edge is greater than the largest cross-sectional dimension, following the Saint-Venant's Principle) and its planeness is verified. Numerical simulations of this member under pure flexion have also shown that after this length ( $0.3m$ ) the results in terms of moment - curvature are homogeneous for all the sections.



(a) 3D view



(b) View at the Shear Force-Bending Moment plane

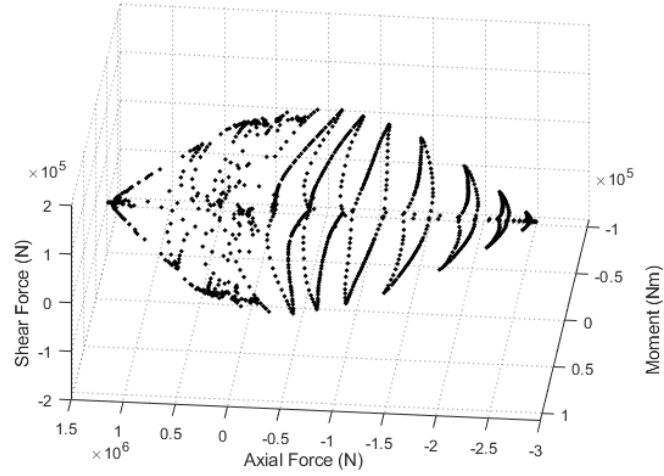


(c) View at the Bending Moment-Axial Force plane

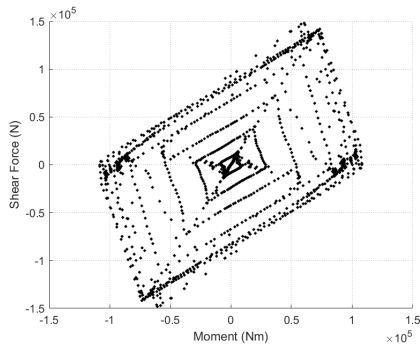
**Fig. 10.** 1<sup>st</sup> characteristic state ('elastic domain'): Interaction diagram (discrete points) obtained by numerical simulations.

## 5. Interaction diagrams for symmetrically reinforced concrete square sections with various reinforcement ratios

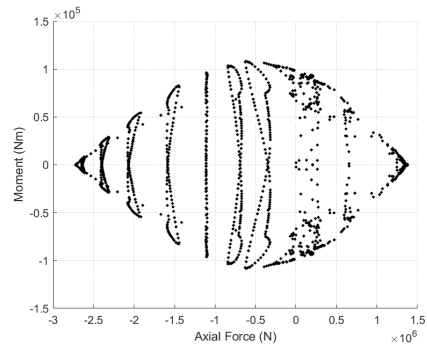
Interaction diagrams are numerically constructed for symmetrically reinforced sections with different reinforcement ratios. The procedure followed is the same



(a) 3D view



(b) View at the Shear Force-Bending Moment plane



(c) View at the Bending Moment-Axial Force plane

**Fig. 11.** 2<sup>nd</sup> characteristic state ('failure'): Interaction diagram (discrete points) obtained by numerical simulations.

as in section 4. The numerical model and the constitutive model parameters are the same as the ones in section 3. The only difference concerns the number of the longitudinal steel bars and their diameter. In Fig. 12 interaction diagrams for the 2<sup>nd</sup> characteristic state of 'failure' are presented for sections M1, M2, M3 (initial model) and M4 for which the reinforcement ratios are 1.01%, 2.01%, 2.57% and

5.15% respectively.

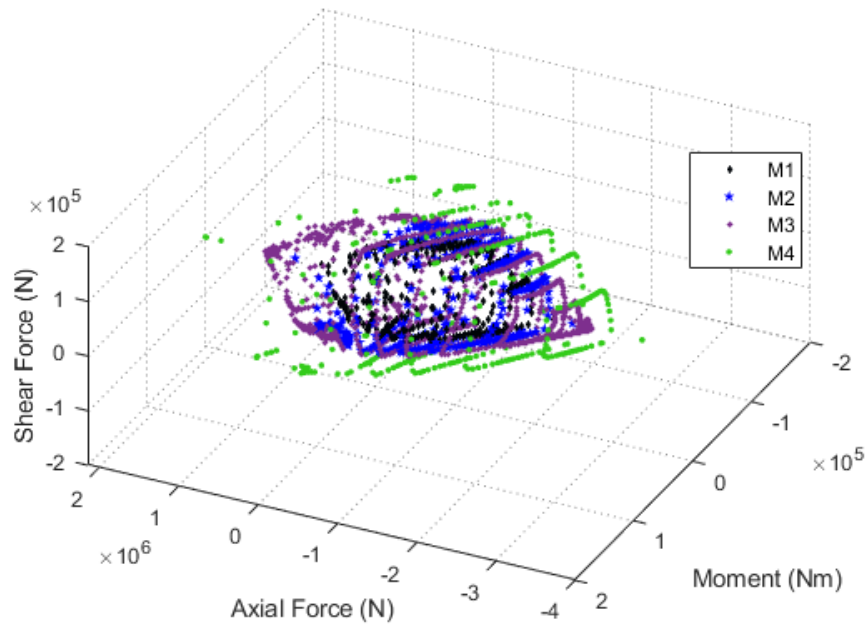


**Fig. 12.** 2<sup>nd</sup> characteristic state ('failure'): Interaction diagrams (discrete points) for sections with different reinforcement ratios obtained by numerical simulations.

It is found that as the reinforcement ratio increases, the failure domain expands, but the form remains similar.

## 6. Analytical expressions of the interaction diagrams

### 6.1 Background

Analytical expressions for the interaction diagrams are very useful for the practitioners to efficiently design reinforced concrete sections. For a robust numerical implementation, these functions should be convex.

Suryasentana et al. [28] proposed a systematic framework employing a restricted set of sum of square convex polynomials for the construction of convex and sufficiently regular functions with the following characteristics: continuity, differentiability with a continuous gradient and Hessian, absence of singularities in the function and in its derivatives and the fact that they always have real values. Odd degree polynomials are excluded because of their lack of convexity. The coefficients of the analytical expression of the failure envelope are computed through a convex optimization problem which minimizes the objective function:

$$F = \sum_{i=1}^n (f(\bar{X}_i^{data}) - 1)^2 \quad (11)$$

subjected to constraint:  $\bar{Y}^\top \nabla^2 f(\bar{X}) \bar{Y}$  is sum of squares for all  $\bar{X}, \bar{Y} \in \text{domain of } f$ , which guarantees that the Hessian  $\nabla^2 f(\bar{X})$  of  $f$  is positive semi-definite. In Eq. 11  $\bar{X}_i^{data}$  is a vector of a discrete failure loading combination points and  $n$  is the number of failure points.

In this work, this procedure is adopted for the identification of the coefficients of the analytical expression and the sum of squares convex optimization problem is solved using YALMIP, a toolbox developed by Lofberg [29] in Matlab together with the SeDuMi semi-definite solver [30].

## 6.2 Computation of the analytical expression at failure ( $2^{nd}$ characteristic state)

The procedure to compute the analytical expressions of the interaction diagram for the limit loading has as follows:

At first, the data of the numerical simulations (section 5) are enriched in order

to be used afterwards as input for the resolution of the sum of squares convex optimization problem. In particular, every set of data of the numerical simulations (for sections M1, M2, M3, M4) are introduced in the following homogeneous polynomial expression of degree 6 (found to provide a good fit) in order to obtain with a non-linear least squares method the coefficients of the polynomial expression for each RC section tested:

$$f_6 = \sum_{\substack{i,j,k=0 \\ |i+j+k|=6}}^6 a_{I(i,j,k)} \bar{N}^i \bar{M}^j \bar{V}^k - 1 \quad (12)$$

This analytical expression, for which the coefficients are calculated, is not guaranteed to be convex. The next step is to use this analytical expression as a tool to obtain further data points, referred as ‘interpolated points’ from now on. These interpolated points are used as input for the resolution of the sum of squares convex optimization problem [28]. More specifically, the interpolated points are standardized in a way that for uniaxial loading conditions their values are 1 (for the positive loading direction) and -1 (for the negative loading direction).

For every set of data (sections M1, M2, M3, M4) two distinct sum of squares convex failure envelopes of the standardized loading variables of degree 4 and 6 are then selected, for which the coefficients need to be identified (Eq. 13 - Eq. 12).

$$f_4 = \sum_{\substack{i,j,k=0 \\ |i+j+k|=4}}^4 a_{I(i,j,k)} \bar{N}^i \bar{M}^j \bar{V}^k - 1 \quad (13)$$

The coefficients of all monomials containing a single loading variable are 1 as

long as the uniaxial loading conditions are applied.

Finally, the objective function is minimized, subjected to the condition of positive semi-definite Hessian. Thus, the coefficients of all monomials are obtained for every set of data (sections M1, M2, M3, M4). The coefficients of the monomials for all the tested sections are presented in Tables 5- 8 for the expression of degree 4 and in Tables 9- 12 for the expression of degree 6.

$a_1$	$a_2$	$a_3$	$a_4$	$a_5$
1	0	5.7	0.01	1
$a_6$	$a_7$	$a_8$	$a_9$	$a_{10}$
0.01	-4.18	-0.01	-2.34	3.24
$a_{11}$	$a_{12}$	$a_{13}$	$a_{14}$	$a_{15}$
0.02	4.71	-0.01	-3.49	1

**Table 5.** M1 section: Coefficients of monomials for the failure envelope expression of degree 4.

$a_1$	$a_2$	$a_3$	$a_4$	$a_5$
1	0	5.87	0	1
$a_6$	$a_7$	$a_8$	$a_9$	$a_{10}$
0.01	-5.26	-0.01	2.36	3.9
$a_{11}$	$a_{12}$	$a_{13}$	$a_{14}$	$a_{15}$
0.02	4.81	-0.02	-3.5	1

**Table 6.** M2 section: Coefficients of monomials for the failure envelope expression of degree 4.

$a_1$	$a_2$	$a_3$	$a_4$	$a_5$
1	0	5.58	0.01	1
$a_6$	$a_7$	$a_8$	$a_9$	$a_{10}$
-0.01	-2.67	-0.03	-2.19	1.23
$a_{11}$	$a_{12}$	$a_{13}$	$a_{14}$	$a_{15}$
0.04	4.76	-0.01	-3.45	1

**Table 7.** M3 section: Coefficients of monomials for the failure envelope expression of degree 4.

$a_1$	$a_2$	$a_3$	$a_4$	$a_5$
1	-0.01	5.88	0.02	1
$a_6$	$a_7$	$a_8$	$a_9$	$a_{10}$
0.01	-3.59	-0.06	-1.8	3.18
$a_{11}$	$a_{12}$	$a_{13}$	$a_{14}$	$a_{15}$
0.05	4.25	-0.03	-3.28	1

**Table 8.** M4 section: Coefficients of monomials for the failure envelope expression of degree 4.

$a_1$	$a_2$	$a_3$	$a_4$	$a_5$	$a_6$	$a_7$
1	0	13.22	0.05	10.07	0.02	1
$a_8$	$a_9$	$a_{10}$	$a_{11}$	$a_{12}$	$a_{13}$	$a_{14}$
0.01	-9.44	-0.04	-10.43	-0.04	-3.39	6.79
$a_{15}$	$a_{16}$	$a_{17}$	$a_{18}$	$a_{19}$	$a_{20}$	$a_{21}$
-0.04	25.72	0.08	10.89	0.01	-17.33	-0.11
$a_{22}$	$a_{23}$	$a_{24}$	$a_{25}$	$a_{26}$	$a_{27}$	$a_{28}$
-15.40	4.56	0.07	12.65	-0.02	-5.5	1

**Table 9.** M1 section: Coefficients of monomials for the failure envelope expression of degree 6.

$a_1$	$a_2$	$a_3$	$a_4$	$a_5$	$a_6$	$a_7$
1	0	14.03	0.03	12.26	0.02	1
$a_8$	$a_9$	$a_{10}$	$a_{11}$	$a_{12}$	$a_{13}$	$a_{14}$
0.01	-12.73	0	-17.97	-0.06	-3.34	8.29
$a_{15}$	$a_{16}$	$a_{17}$	$a_{18}$	$a_{19}$	$a_{20}$	$a_{21}$
-0.05	35.83	0.13	11.09	0	-22.46	-0.18
$a_{22}$	$a_{23}$	$a_{24}$	$a_{25}$	$a_{26}$	$a_{27}$	$a_{28}$
15.42	5.56	0.1	12.69	-0.02	-5.51	1

**Table 10.** M2 section: Coefficients of monomials for the failure envelope expression of degree 6.

$a_1$	$a_2$	$a_3$	$a_4$	$a_5$	$a_6$	$a_7$
1	0.02	12.56	0.02	9.41	0.02	1
$a_8$	$a_9$	$a_{10}$	$a_{11}$	$a_{12}$	$a_{13}$	$a_{14}$
-0.02	-9.38	-0.01	-6.44	-0.06	-3.27	5.34
$a_{15}$	$a_{16}$	$a_{17}$	$a_{18}$	$a_{19}$	$a_{20}$	$a_{21}$
-0.03	10.68	0.09	11.17	0	-4.31	-0.11
$a_{22}$	$a_{23}$	$a_{24}$	$a_{25}$	$a_{26}$	$a_{27}$	$a_{28}$
-15.26	0.48	0.06	12.56	-0.01	-5.44	1

**Table 11.** M3 section: Coefficients of monomials for the failure envelope expression of degree 6.

### 6.3 Comparison of different analytical expressions at failure ( $2^{nd}$ characteristic state)

In order to choose the analytical expression of the failure envelope for a given reinforced concrete section, in the following Figs. 13, 14, 15 we present 2D sections of the failure envelope in the moment - axial force, shear force - moment and shear force - axial force planes, together with the data obtained by the numerical simulations and the interpolated data for the RC section M3.

$\mathbf{a}_1$	$\mathbf{a}_2$	$\mathbf{a}_3$	$\mathbf{a}_4$	$\mathbf{a}_5$	$\mathbf{a}_6$	$\mathbf{a}_7$
1	0	11.76	0.09	8.58	0.03	1
$\mathbf{a}_8$	$\mathbf{a}_9$	$\mathbf{a}_{10}$	$\mathbf{a}_{11}$	$\mathbf{a}_{12}$	$\mathbf{a}_{13}$	$\mathbf{a}_{14}$
0	-10.18	-0.15	-2.36	-0.08	-2.11	7.74
$\mathbf{a}_{15}$	$\mathbf{a}_{16}$	$\mathbf{a}_{17}$	$\mathbf{a}_{18}$	$\mathbf{a}_{19}$	$\mathbf{a}_{20}$	$\mathbf{a}_{21}$
0.04	16.67	0.14	8.54	-0.02	-12.25	-0.18
$\mathbf{a}_{22}$	$\mathbf{a}_{23}$	$\mathbf{a}_{24}$	$\mathbf{a}_{25}$	$\mathbf{a}_{26}$	$\mathbf{a}_{27}$	$\mathbf{a}_{28}$
-12.57	3.68	0.1	11.07	-0.02	-5.14	1

**Table 12.** M4 section: Coefficients of monomials for the failure envelope expression of degree 6.

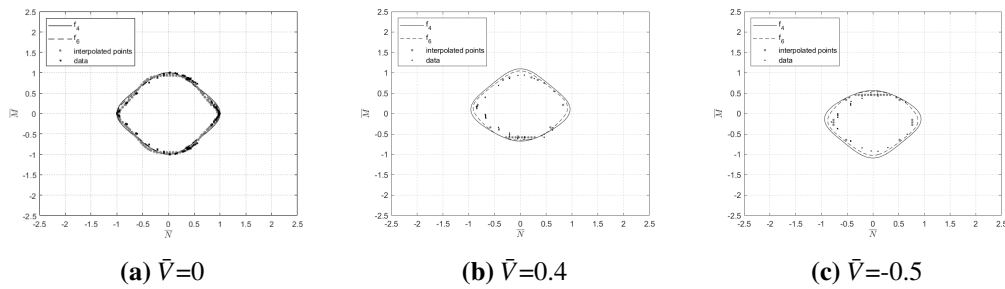


**Fig. 13.** M3 section: Moment - axial force interaction diagrams obtained by polynomials  $f_4$ ,  $f_6$  compared to data by numerical simulations and interpolated points.

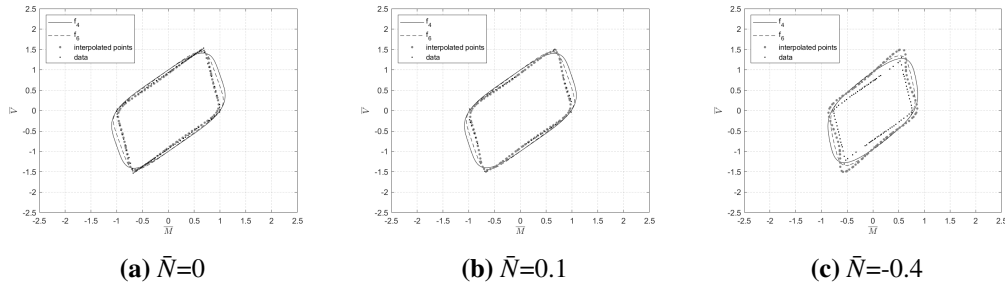


**Fig. 14.** M3 section: Moment - shear force interaction diagrams obtained by polynomials  $f_4$ ,  $f_6$  compared to data by numerical simulations and interpolated points.

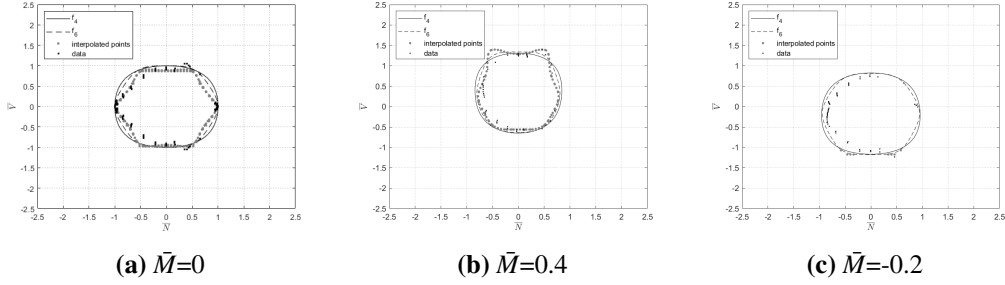


**Fig. 15.** M3 section: Axial force - shear force interaction diagrams obtained by polynomials  $f_4$ ,  $f_6$  compared to data by numerical simulations and interpolated points.

It can be clearly seen that the polynomial of degree 6 gives a better approximation of the failure envelope. In particular the sum of squares convex optimization problem is solved for the RC section M3 with an overall precision of  $1.1 \text{ e}^{-6}$  for the polynomial of degree 4 and a precision of  $9.4 \text{ e}^{-10}$  for the polynomial of degree 6. The corresponding figures for the sections M1, M2 and M4 can be found in Appendix C where one can observe that the conclusions are similar. Fig. 16 presents the failure envelope of degree 6 in the 3D space of the RC section M3.

#### 6.4 Computation of the analytical expression of the domain of elasticity (1st characteristic state)

The procedure to compute the analytical expression of the interaction diagram for the 1<sup>st</sup> characteristic state is different than the one of section 6.2. In particular, the interaction diagram for the 1<sup>st</sup> characteristic state (Fig. 10) presents similar form to the one for the 2<sup>nd</sup> characteristic state (Fig. 11) but the centers of the two surfaces are offset to each other. Thus, the proposed analytical expression for the 1<sup>st</sup> characteristic state is the same as Eq. 12 but the standardized variables  $\bar{N}$ ,  $\bar{M}$ ,  $\bar{V}$

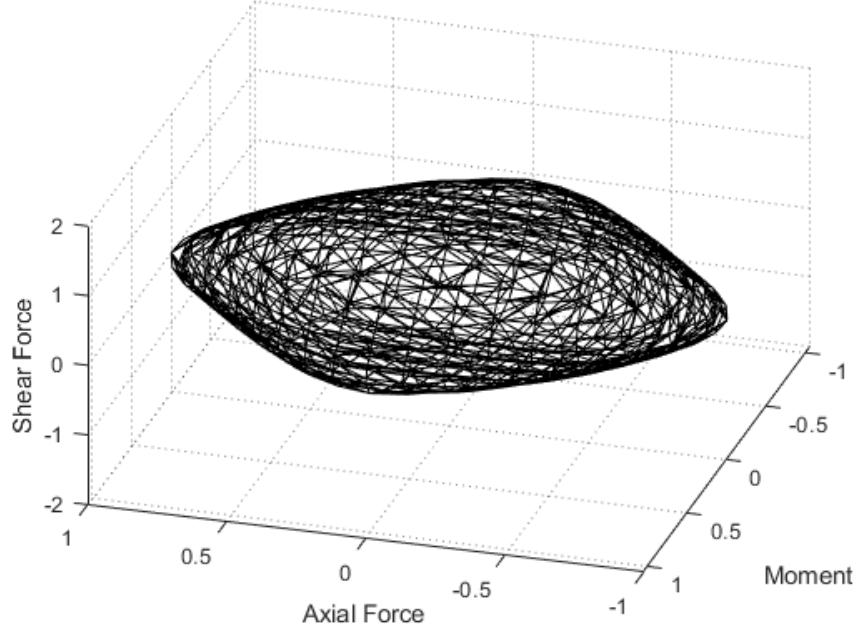


**Fig. 16.** Failure envelope in 3D standardized space for the RC section M3.

are replaced by  $\frac{\bar{N}-\bar{N}_0}{\bar{N}^*}$ ,  $\frac{\bar{M}-\bar{M}_0}{\bar{M}^*}$ ,  $\frac{\bar{V}-\bar{V}_0}{\bar{V}^*}$  respectively in order to modify the center and the radii of the ellipsoid of the 2<sup>nd</sup> characteristic state. The analytical expression for the 1<sup>st</sup> characteristic state is given by Eq. 14 for which the coefficients of all monomials are already calculated and presented in Tables 9- 12 for the RC sections M1, M2, M3 and M4.

$$f_6 = \sum_{\substack{i,j,k=0 \\ |i+j+k|=6}}^6 a_{I(i,j,k)} \left( \frac{\bar{N}-\bar{N}_0}{\bar{N}^*} \right)^i \left( \frac{\bar{M}-\bar{M}_0}{\bar{M}^*} \right)^j \left( \frac{\bar{V}-\bar{V}_0}{\bar{V}^*} \right)^k - 1 \quad (14)$$

Each set of data points that correspond to the 1<sup>st</sup> characteristic state (Fig. 10) are subsequently introduced in Eq. 14. The center ( $\bar{N}_0, \bar{M}_0, \bar{V}_0$ ) and the radii ( $\bar{N}^*, \bar{M}^*, \bar{V}^*$ ) of the ellipsoid corresponding to the 1<sup>st</sup> characteristic state are calculated by the resolution of a non-linear least squares optimization problem. The obtained values for the RC sections M1, M2, M3 and M4 are presented in Table 13. Fig. 17 presents both characteristic states of degree 6 in the 3D space for the RC section M3. The corresponding figures for the sections M1, M2 and M4 can be found in Appendix D.

RC section	$\bar{N}_0$	$\bar{M}_0$	$\bar{V}_0$	$\bar{N}^*$	$\bar{M}^*$	$\bar{V}^*$
M1	-0.0117	0.0000	-0.0003	0.7435	0.6096	0.6366
M2	-0.0346	0.0000	-0.0002	0.7783	0.8598	0.9427
M3	-0.1101	0.0001	0.0000	0.7590	0.8236	0.8517
M4	-0.0505	0.0001	0.0000	0.7658	0.8751	0.9514

**Table 13.** Center and radii of the ellipsoid corresponding to the 1<sup>st</sup> characteristic state.

### 6.5 Summary of the steps for the calculation of the analytical expressions of the two characteristic states

The general procedure for the derivation of the analytical expressions of the two characteristic states is briefly summarized in the following steps:

- enrichment of the data points of the 2<sup>nd</sup> characteristic state from the numerical simulations
- standardization of the enriched data points of the 2<sup>nd</sup> characteristic state

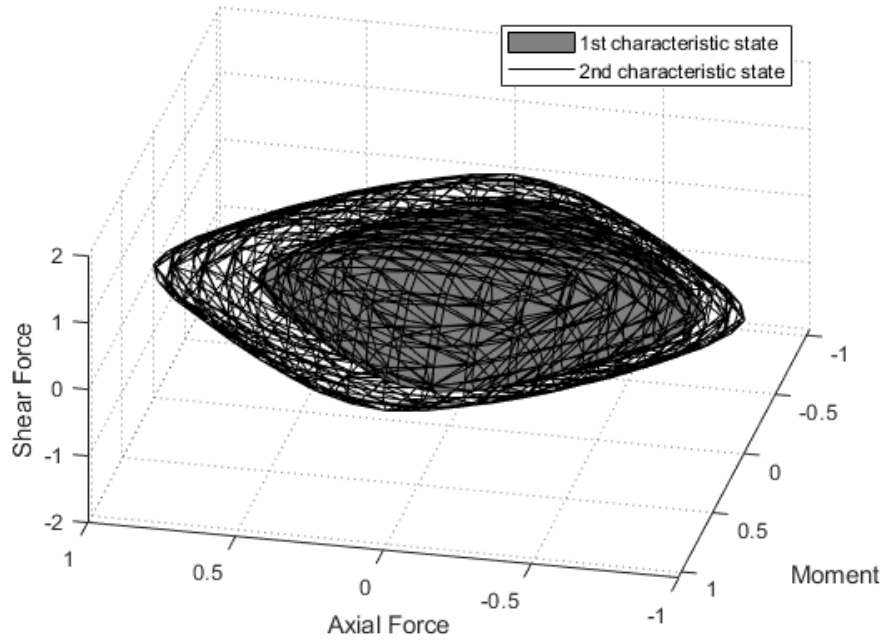


**Fig. 17.** M3 section: 1<sup>st</sup> and 2<sup>nd</sup> characteristic states in 3D standardized space.

- resolution of the sum of squares convex optimization problem for the chosen homogeneous polynomial expressions in order to obtain the coefficients of all monomials
- standardization of the data points of the 1<sup>st</sup> characteristic state from the numerical simulations; these data are used as input in the next step
- computation of the analytical expression of the 1<sup>st</sup> characteristic state using the same expression of the 2<sup>nd</sup> characteristic state by changing the center and the radii of the ellipsoid

### 6.6 *Comparison with existing interaction diagrams from the Eurocode*

For the 2D swipe tests, in the moment - axial force space, a comparison of the failure surface (obtained by numerical simulations) to the one obtained by applying the methodology found in Eurocode is provided in Fig. 18 for the RC section M3. The corresponding figures for the sections M1, M2 and M4 can be found in Appendix E. At each Figure, the surface obtained by the method described in Eurocode without applying the security coefficients is also provided.

It can be observed that all surfaces obtained by finite element simulations and by the methodology described in Eurocode present similar forms. Furthermore, as expected, the surface obtained by Eurocode underestimates the points of failure. More specifically, for the combined flexion to traction area the ultimate longitudinal strain of the steel bars is fixed to 7.5%, as stated before. This criterion allows for obtaining a less conservative interaction diagram, compared to the one provided by the methodology in Eurocode which (i) considers as an ultimate limit the point at which steel reaches its elastic limit in tension and (ii) ignores the tensile strength of concrete. The choice of such a less conservative criterion can be beneficial for applications in civil engineering as it can offer the option of a more economical design of reinforced concrete structures.

For the combined flexion to compression region, the numerically produced surface presents a good fit to the curve obtained by the method of Eurocode without application of security coefficients.

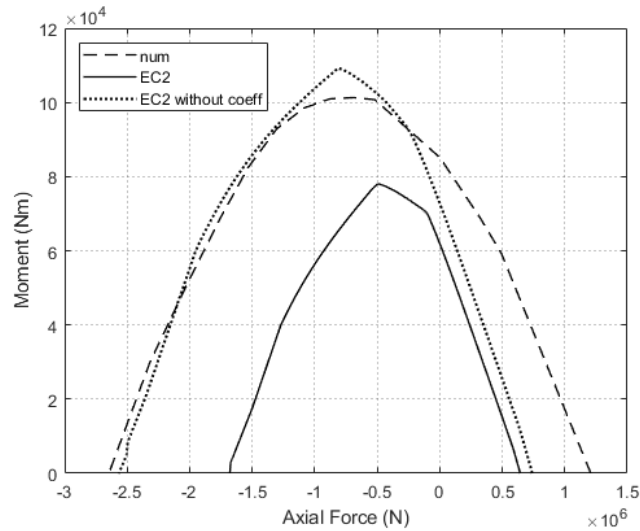


**Fig. 18.** Moment - axial force interaction diagram for M3 RC section. Comparison to the one obtained by the method in Eurocode with and without the application of the security coefficients.

## 7. Conclusions

In this article a numerical methodology is presented on the construction of failure envelopes for given symmetrically RC square sections with various reinforcement ratios. Suitable constitutive models are first chosen for the description of the material behavior, both for concrete and steel. The choice of a 3D finite element modeling leads to more precise results as there are no kinematical assumptions as in classical beam finite element calculations. Finally, a methodology is provided to derive analytical expressions of two characteristics states based on the numerical results.

Further investigating factors, such as steel strength, concrete compressive strength, consideration of non-perfect bonding between concrete and steel, ratio and posi-

tion of the longitudinal and transversal reinforcement, section geometry and shape should be examined in order to provide more complete research results. The 3D calculations being however extremely costly, as more than 1428000 core hours of computational time were necessary to obtain the presented interaction diagrams (the calculations took place using the supercomputer Liger of the Centrale Nantes SuperComputing Center. Liger is a BULL/Atos DLC720 cluster of 252 compute nodes and 14 visualization nodes with 24 cores per node and a total compute memory of 36608GB.), this can be the scope of future work.

### **Acknowledgments**

The authors would like to gratefully acknowledge Dr Stephen Suryasentana for his contribution to the computation of the analytical expression of the failure envelope, by providing a code example of the application of the methodology described in [28]. The authors would also like to thank Pr Stathis Bousias from the University of Patras (Greece) for providing the experimental results of the reinforced concrete column. The first author would like to acknowledge the financial support of Groupe Essor for funding her Cifre PhD.

### **Appendix A. About the additional stiffness**

The chosen mesh discretization results to an additional stiffness. To verify the influence of this additional stiffness on the global response, two finite element models are built for a comparative study of a reinforced concrete beam under

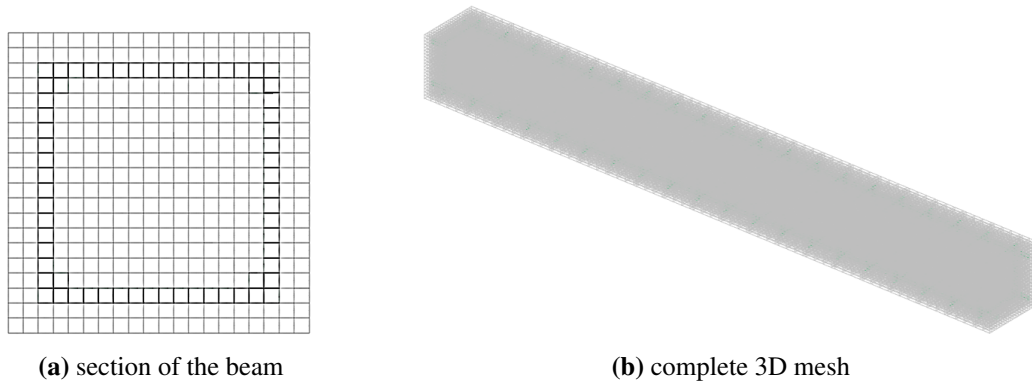
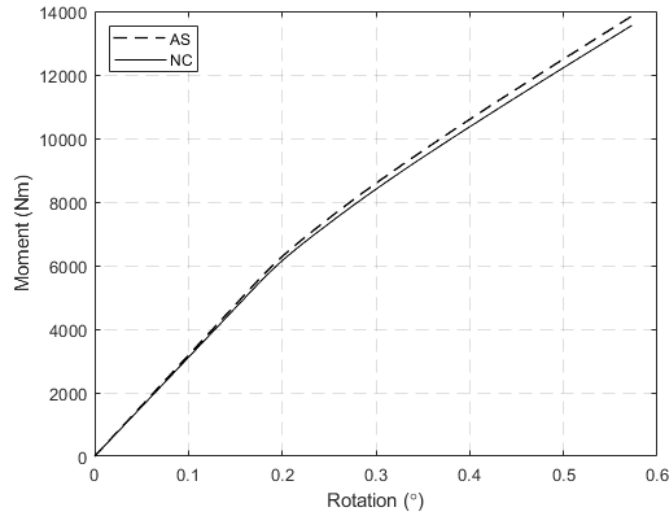


**Fig. A.19.** Beam mesh.

flexion. The dimensions of the beam are 0.2m/0.2m/2m. Four reinforcing steel bars of a diameter of 10mm are symmetrically distributed in the beam section. Transversal reinforcing steel stirrups of a diameter of 10mm are distributed every 100mm in the length of the beam. The concrete cover is taken equal to 20mm. The first finite element model (AS) is constructed by imposing displacement compatibility between steel and concrete meshes. The second finite element model (NC) is constructed in a way that every single node of different elements coincides with the nodes of the other elements. Therefore, for geometrical convenience the steel bars are modelled by a rectangular section. The mesh of the beam is presented in Fig. A.19.

The beam is considered fixed on its edge and on the other edge a displacement controlled flexural load is applied as a linear distribution of axial displacements, varying according to the distance of each node from the centroid of the section. The global response in terms of moment - rotation is obtained for both cases and is shown in Fig. A.20. It is found that the influence of the additional stiffness of

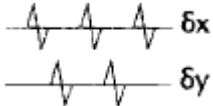
the first type of modeling (AS) on the global response of the beam can be ignored.



**Fig. A.20.** Comparison of global responses; AS: modeling technique providing an additional stiffness and NC: modeling technique where the nodes of different components coincide

## Appendix B. Comparison of different meshes

In order to optimize computational time, a comparison between the numerical results obtained with different mesh refinements with reference to the experimental data is shown hereafter (S1 test). The loading program of S1 is presented in Table B.14. The parameters for the concrete constitutive law are listed in Table 2 and Table B.15 and for steel in Table 4. Two meshes of 10560 (Fig. B.21) and 31560 (Fig. B.22) 3D finite elements are adopted. At the section, the finite element size is 0.025m for the coarse mesh and 0.0125m for the fine mesh. The two meshes provide similar results as shown in Fig. B.23. All calculations are

Test Specimen	$f'_c$	$N/(A_c f'_c)$	Load Path
S1	29.0	0.12	

**Table B.14.** Test specimen S1, compressive strength, applied axial load and transversal load (schematically).

therefore conducted with the coarse mesh.

Parameter	$\sigma_{c1}$	$\sigma_{c2}$
Description	Stress of point 1	Stress of point 2
SI Unit	<i>MPa</i>	<i>MPa</i>
S1	-25.4	-24.4

**Table B.15.** RC columns: parameters for concrete (varying for each test).

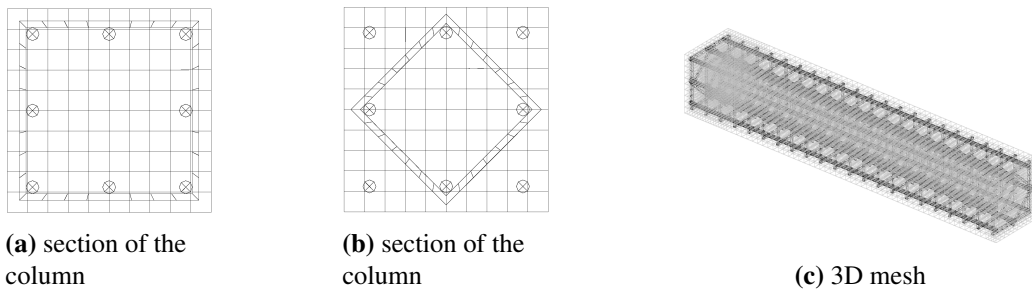


**Fig. B.21.** Coarse mesh.

### Appendix C. Comparison of different analytical expressions at failure (2<sup>nd</sup> characteristic state) for the RC sections M1, M2 and M4

2D sections of the failure envelope in the moment - axial force, shear force - moment and shear force - axial force planes, together with the data obtained by

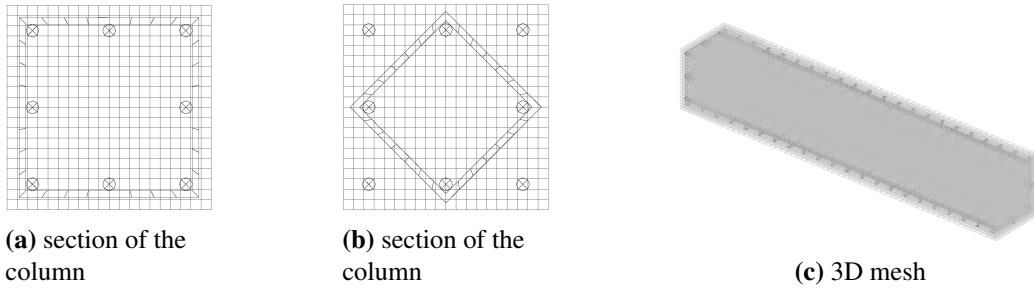


**Fig. B.22.** Fine mesh.

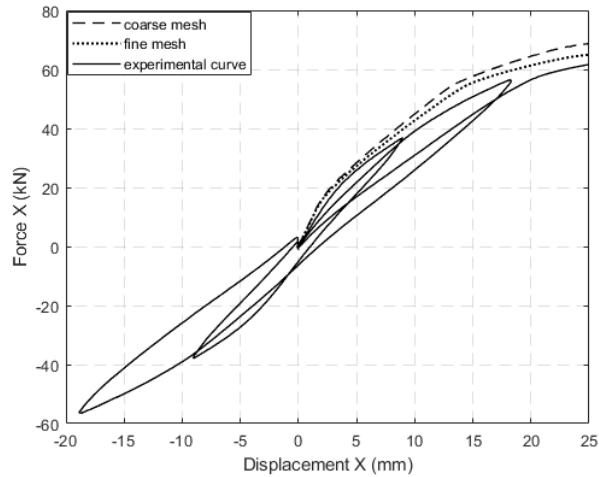


**Fig. B.23.** Test S1: comparison of the responses of the coarse and fine meshes with the experimental results.

the numerical simulations and the interpolated data for the RC section M1 are presented in Figs. C.24, C.25, C.26, for the section M2 in Figs. C.27, C.28, C.29 and for the section M4 in Figs. C.30, C.31, C.32.

As stated in section 6.3, polynomial expressions of degree 6 ( $f_6$ ) give better approximations of the failure envelopes. For the RC section M1, the precision of the resolution of the sum of squares convex optimization problem is  $5.9e-7$  for the polynomial of degree 4 ( $f_4$ ) and  $5.1e-9$  for the polynomial of degree 6 ( $f_6$ ).

For the RC section M2, the precision is  $1.1 \text{ e}-6$  for the polynomial of degree 4 and  $5.1 \text{ e}-10$  for the polynomial of degree 6 and for the RC section M4, the precision is  $1.2 \text{ e}-7$  for the polynomial of degree 4 and  $5.8 \text{ e}-10$  for the polynomial of degree 6.

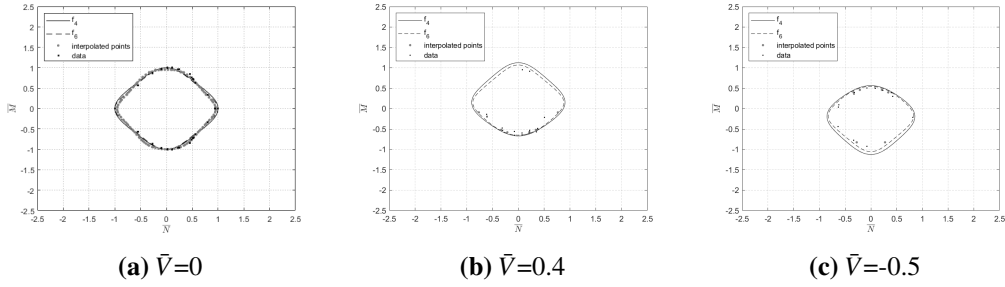


**Fig. C.24.** M1 section: Moment - axial force interaction diagrams obtained by polynomials  $f_4$ ,  $f_6$  compared to data by numerical simulations and interpolated points.

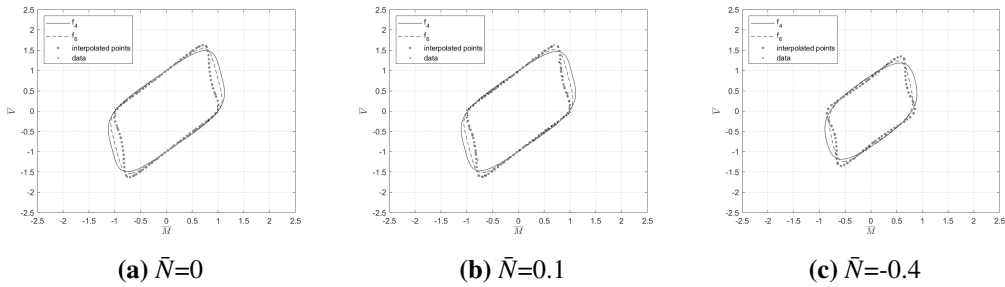


**Fig. C.25.** M1 section: Moment - shear force interaction diagrams obtained by polynomials  $f_4$ ,  $f_6$  compared to data by numerical simulations and interpolated points.

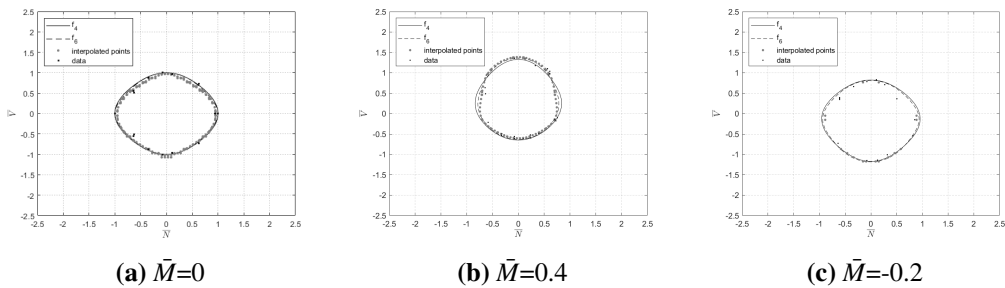


**Fig. C.26.** M1 section: Axial force - shear force interaction diagrams obtained by polynomials  $f_4$ ,  $f_6$  compared to data by numerical simulations and interpolated points.

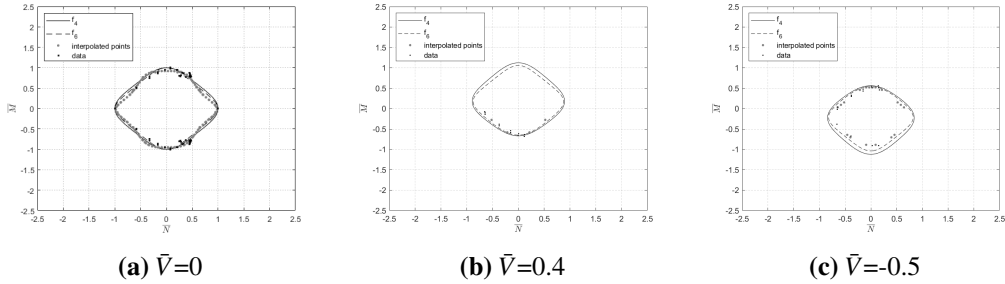


**Fig. C.27.** M2 section: Moment - axial force interaction diagrams obtained by polynomials  $f_4$ ,  $f_6$  compared to data by numerical simulations and interpolated points.

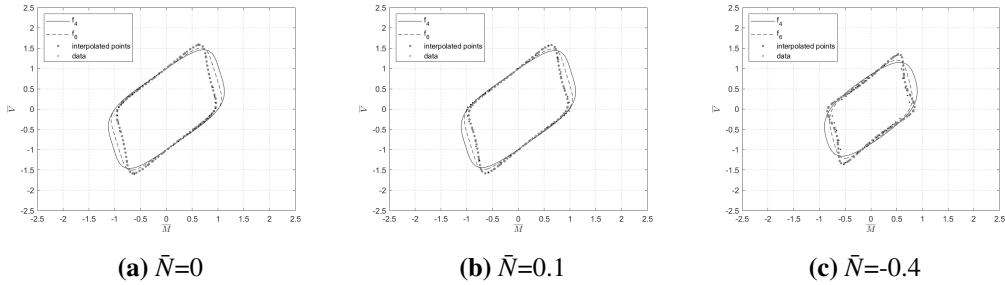


**Fig. C.28.** M2 section: Moment - shear force interaction diagrams obtained by polynomials  $f_4$ ,  $f_6$  compared to data by numerical simulations and interpolated points.

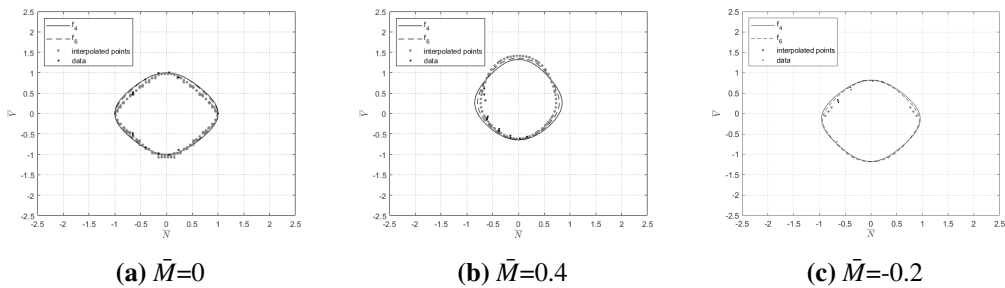


**Fig. C.29.** M2 section: Axial force - shear force interaction diagrams obtained by polynomials  $f_4$ ,  $f_6$  compared to data by numerical simulations and interpolated points.

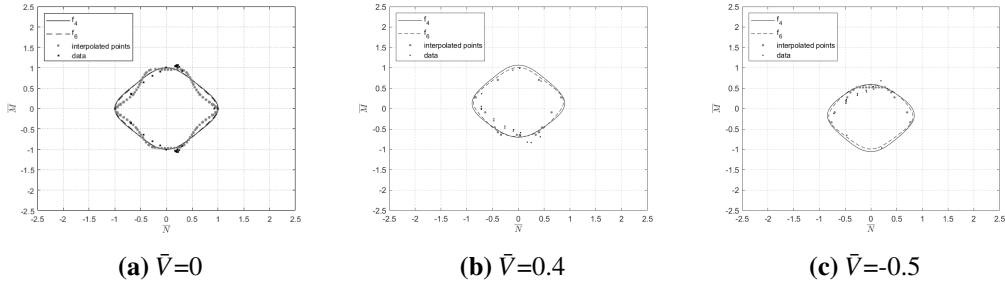


**Fig. C.30.** M4 section: Moment - axial force interaction diagrams obtained by polynomials  $f_4, f_6$  compared to data by numerical simulations and interpolated points.

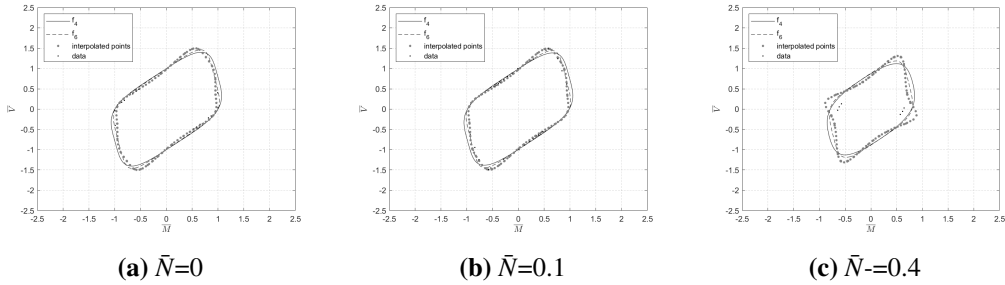


**Fig. C.31.** M4 section: Moment - shear force interaction diagrams obtained by polynomials  $f_4, f_6$  compared to data by numerical simulations and interpolated points.

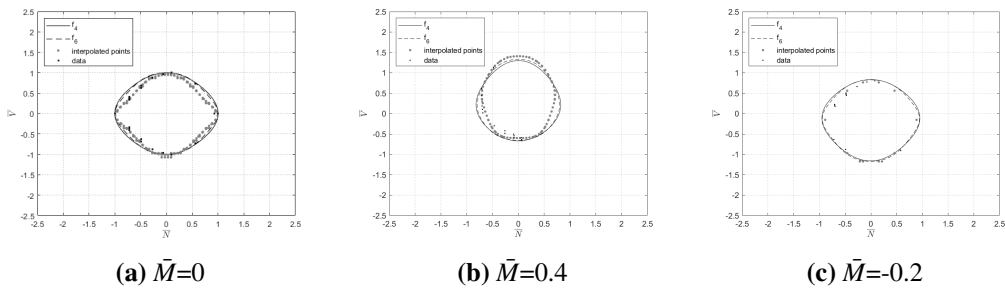


**Fig. C.32.** M4 section: Axial force - shear force interaction diagrams obtained by polynomials  $f_4, f_6$  compared to data by numerical simulations and interpolated points.

**Appendix D. 1<sup>st</sup> and 2<sup>nd</sup> characteristic state in 3D standardized space for the RC sections M1, M2 and M4**

In this Appendix both characteristic states of degree 6 in the standardized 3D space for the sections M1, M2 and M4 are presented in Fig. D.33, Fig. D.34 and Fig. D.35 respectively.

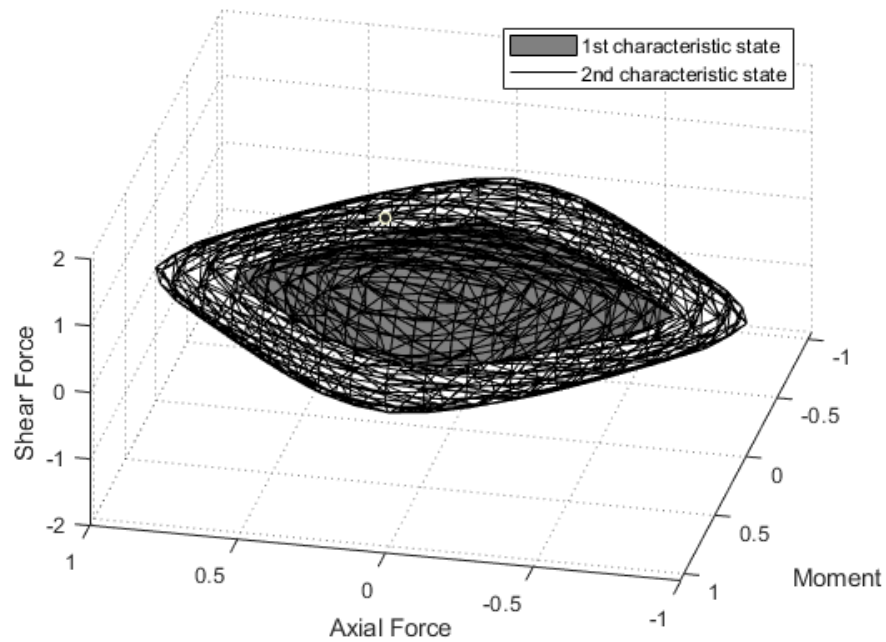


**Fig. D.33.** M1 section: 1<sup>st</sup> and 2<sup>nd</sup> characteristic states in 3D standardized space.

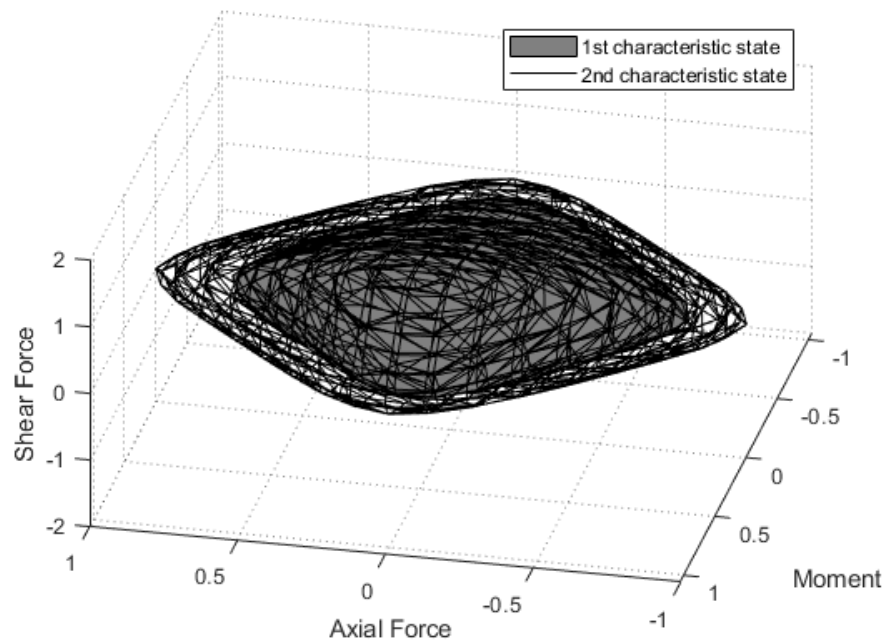


**Fig. D.34.** M2 section: 1<sup>st</sup> and 2<sup>nd</sup> characteristic states in 3D standardized space.

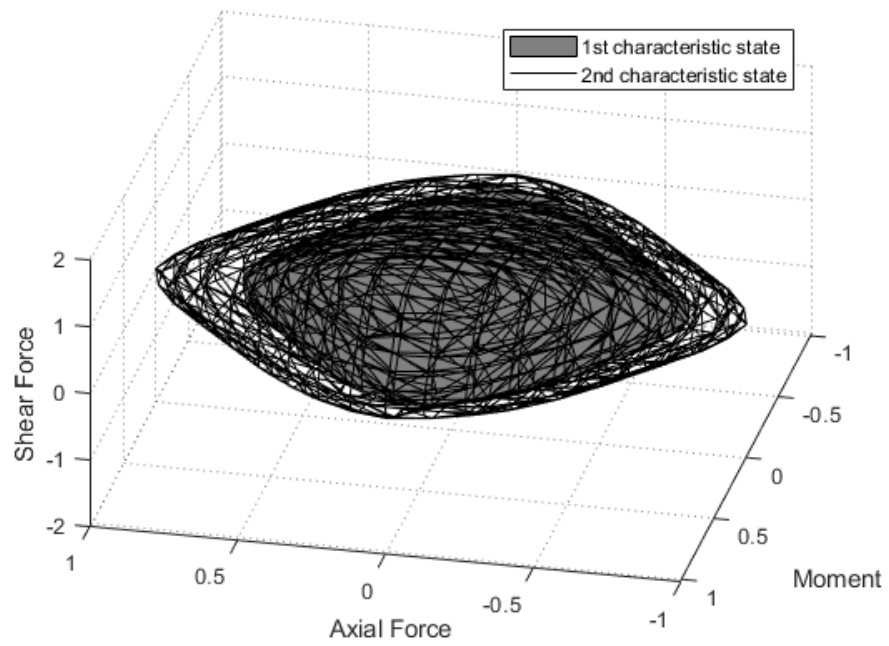


**Fig. D.35.** M4 section: 1<sup>st</sup> and 2<sup>nd</sup> characteristic states in 3D standardized space.

## Appendix E. Comparison with existing interaction diagrams from the Eurocode for the RC sections M1, M2 and M4

In this Appendix comparisons of the failure surfaces (obtained by numerical simulations) to the ones obtained by applying the methodology found in Eurocode are presented for the RC sections M1, M2 and M4 in Fig. E.36, Fig. E.37 and Fig. E.38 respectively.

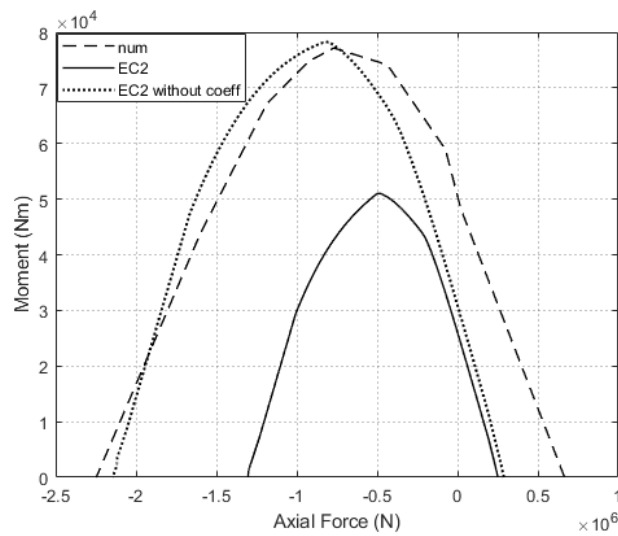


**Fig. E.36.** Moment - axial force interaction diagram for M1 RC section. Comparison to the one obtained by the method in Eurocode with and without the application of the security coefficients.

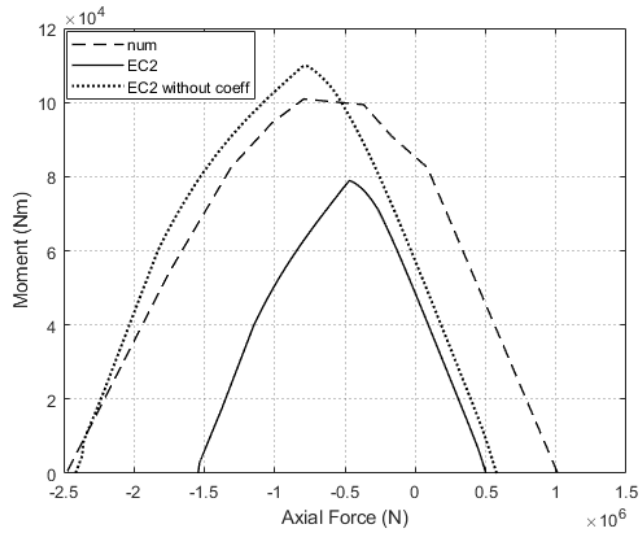


**Fig. E.37.** Moment - axial force interaction diagram for M2 RC section. Comparison to the one obtained by the method in Eurocode with and without the application of the security coefficients.

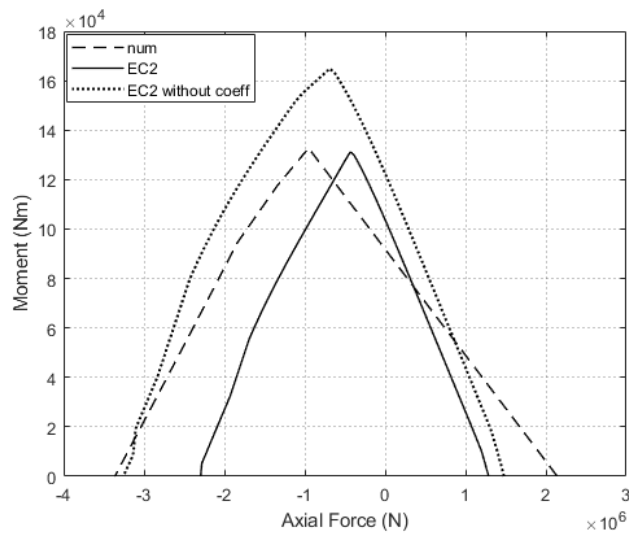


**Fig. E.38.** Moment - axial force interaction diagram for M4 RC section. Comparison to the one obtained by the method in Eurocode with and without the application of the security coefficients.

## References

- [1] Eurocode, Eurocode 2: Design of concrete structures: Part 1-1: General rules and rules for buildings, British Standards Institution, 2004.
- [2] J. Salençon, Calcul à la rupture et analyse limite, Presses de l'Ecole Nationale des Ponts et Chaussées, Paris, 1983.
- [3] P. Kœchlin, Modèle de comportement membrane-flexion et critère de perforation pour l'analyse de structures minces en béton armé sous choc mou, These de doctorat, Ecole Polytechnique (2007).
- [4] P. Koechlin, S. Andrieux, A. Millard, S. Potapov, Failure criterion for reinforced concrete beams and plates subjected to membrane force, bending and shear, *European Journal of Mechanics-A/Solids* 27 (6) (2008) 1161–1183.
- [5] S. M. Elachachi, Sur l'elaboration d'une methode simplifiee d'analyse des structures de genie civil par macro-elements adaptes aux constructions composites et endommageables, Ph.D. thesis, Paris 6 (1992).
- [6] F. J. Vecchio, M. P. Collins, Predicting the response of reinforced concrete beams subjected to shear using modified compression field theory, *ACI Structural Journal* 85 (3) (1988) 258–268.
- [7] F. J. Vecchio, M. P. Collins, The modified compression-field theory for reinforced concrete elements subjected to shear., *ACI J.* 83 (2) (1986) 219–231.
- [8] K. N. Rahal, Shear strength of reinforced concrete: Part 1-membrane elements subjected to pure shear, *ACI Structural Journal* 97 (1) (2000) 86–93.
- [9] K. N. Rahal, Shear strength of reinforced concrete: Part ii—beams subjected

- to shear, bending moment, and axial load, *Structural Journal* 97 (2) (2000) 219–224.
- [10] T.-A. Nguyen, Development of an enhanced finite element model for reinforced concrete members subjected to combined shear-bending-torsion actions, Ph.D. thesis, INSA Rennes (2019).
- [11] A. Carpinteri, M. Corrado, G. Goso, M. Paggi, Size-scale effects on interaction diagrams for reinforced concrete columns, *Construction and Building Materials* 27 (1) (2012) 271–279.
- [12] R. Nova, L. Montrasio, Settlements of shallow foundations on sand, *Géotechnique* 41 (2) (1991) 243–256.
- [13] S. Grange, P. Kotronis, J. Mazars, A macro-element to simulate 3d soil–structure interaction considering plasticity and uplift, *International Journal of Solids and Structures* 46 (20) (2009) 3651–3663.
- [14] C. Cremer, A. Pecker, L. Davenne, Elaboration of a ssi macro-element with uplift of shallow foundation, in: *Implications Of Recent Earthquakes On Seismic Risk*, World Scientific, 2000, pp. 127–138.
- [15] Z. Li, P. Kotronis, S. Escoffier, Numerical study of the 3d failure envelope of a single pile in sand, *Computers and Geotechnics* 62 (2014) 11–26.
- [16] Z. Li, P. Kotronis, S. Escoffier, C. Tamagnini, A hypoplastic macroelement for single vertical piles in sand subject to three-dimensional loading conditions, *Acta Geotechnica* 11 (2) (2016) 373–390.
- [17] Z. Li, P. Kotronis, S. Escoffier, C. Tamagnini, A hypoplastic macroelement formulation for single batter piles in sand, *International Journal for Numeri-*

- cal and Analytical Methods in Geomechanics 42 (12) (2018) 1346–1365.
- [18] S. N. Bousias, G. Verzeletti, M. N. Fardis, E. Gutierrez, Load-path effects in column biaxial bending with axial force, *Journal of Engineering Mechanics* 121 (5) (1995) 596–605.
- [19] R. Faria, J. Oliver, M. Cervera, A strain-based plastic viscous-damage model for massive concrete structures, *International Journal of Solids and Structures* 35 (14) (1998) 1533–1558.
- [20] A. Hillerborg, M. Mod er, P.-E. Petersson, Analysis of crack formation and crack growth in concrete by means of fracture mechanics and finite elements, *Cement and Concrete Research* 6 (6) (1976) 773–781.
- [21] Z. P. Baant, B. H. Oh, Crack band theory for fracture of concrete, *Mat riaux et Construction* 16 (3) (1983) 155–177.
- [22] H. Kupfer, H. K. Hilsdorf, H. Rusch, Behavior of concrete under biaxial stresses, *ACI Structural Journal* 66 (8) (1969) 656–666.
- [23] E. Gutierrez, G. Magonette, G. Verzeletti, Experimental studies of loading rate effects on reinforced concrete columns, *Journal of Engineering Mechanics* 119 (5) (1993) 887–904.
- [24] Cast3M, Description of the finite element code cast3m, <http://www-cast3m.cea.fr>.
- [25] R. Faria, Avaliao do comportamento s smico de barragens de bet o atrav s de um modelo de dano cont nuo, Ph.D. thesis, Faculdade de Engenharia da Universidade do Porto (1994).
- [26] E. Faccioli, M. Vanini, R. Paolucci, TRISEE: 3D site effects and soil-

foundation interaction in earthquake and vibration risk evaluation, European commission. Directorate-general 12. Science, research and development, 1999.

- [27] S. Grange, P. Kotronis, J. Mazars, A macro-element for a circular foundation to simulate 3d soil–structure interaction, *International Journal for Numerical and Analytical Methods in Geomechanics* 32 (10) (2008) 1205–1227.
- [28] S. Suryasentana, H. Burd, B. Byrne, A. Shonberg, A systematic framework for formulating convex failure envelopes in multiple loading dimensions, *Géotechnique* 70 (4) (2019).
- [29] J. Lofberg, Yalmip: A toolbox for modeling and optimization in matlab, in: 2004 IEEE international conference on robotics and automation (IEEE Cat. No. 04CH37508), IEEE, 2004, pp. 284–289.
- [30] J. F. Sturm, Using sedumi 1.02, a matlab toolbox for optimization over symmetric cones, *Optimization Methods and Software* 11 (1-4) (1999) 625–653.